

**MBE GROWTH OF 2D MoTe₂ AND HETEROSTRUCTURES
WITH INVESTIGATIONS ON PHASE ENGINEERING AND
CHARGE TRANSFER EFFECTS**

KAMLESH



**DEPARTMENT OF PHYSICS
INDIAN INSTITUTE OF TECHNOLOGY DELHI
JANUARY 2026**

© Indian Institute of Technology Delhi (IITD), New Delhi, 2026

**MBE GROWTH OF 2D MoTe₂ AND HETEROSTRUCTURES
WITH INVESTIGATIONS ON PHASE ENGINEERING AND
CHARGE TRANSFER EFFECTS**

by

KAMLESH

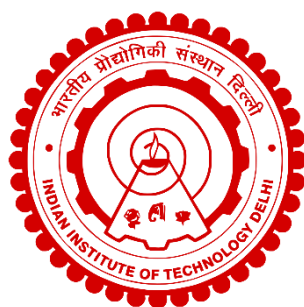
DEPARTMENT OF PHYSICS

Submitted

in fulfilment of requirements of degree of

Doctor of Philosophy

to the



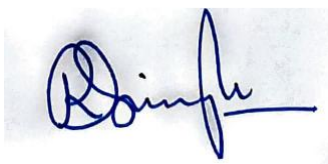
INDIAN INSTITUTE OF TECHNOLOGY DELHI

January 2026

*To my parents, Shri Jaikishan and Smt. Kamla,
and my sister Sunanda*

Certificate

This is to certify that the thesis entitled “**MBE Growth of 2D MoTe₂ and Heterostructures With Investigations on Phase Engineering and Charge Transfer Effects**” submitted by **Mr. Kamlesh**, a research scholar in the *Department of Physics*, Indian Institute of Technology Delhi for the award of the degree of **Doctor of Philosophy**, is a record of original and bonafide research work carried out by him. He has worked under my guidance and supervision, and has fulfilled the requirements, which, to my knowledge, have reached the requisite standard for the submission of the thesis. The results contained in it have not been submitted in part or in full to any other university or institute for the award of any degree or diploma.



Prof. Rajendra Singh

Department of Physics
Indian Institute of Technology Delhi
New Delhi-110016
India

Date: January 30, 2026

Acknowledgements

This Ph.D. journey has been like living a mini full life. Most of the time, it has been joyful and full of confidence, while other times it has come up with hard challenges. However, the presence of some special people in this journey has been that guiding light and source of positive energy for me to overcome the challenges and move forward to the next stage. It is really a precious feeling for me as I get the opportunity to present my gratitude to all these people who, academically or personally, have influenced and contributed positively to this work. This thesis would have never been in its present form without the support and encouragement of these people.

Firstly, I would like to express my sincere gratitude to my Ph.D. advisor, **Prof. Rajendra Singh**. It was an honor for me to carry out my work under his supervision. He has directly and indirectly taught me how to proceed with the Ph.D. research, problem selection and even time management during Ph.D. in the most realistic way possible. I am very grateful to him for providing the valuable experimental suggestions, pushing to address the research problems and importantly, for providing freedom to execute my plans, which comes from his belief in me. I remember him emphasizing the importance of having a set of goals in almost every meeting, which has been a key for me. I appreciate all of his contributions of valuable time, suggestions, evaluation, collaborations and research funding, to make this thesis work very impactful and stimulating. Finally, I would like to extend my special thanks to him for choosing me to work with the MBE and for showing his belief in me to take the responsibility of setting up the MBE lab.

In addition to my supervisor, I would like to sincerely thank my Ph.D. research committee members **Prof. J. P. Singh, Prof. Pankaj Srivastava** and **Prof. Samaresh Das** for assessing my work time to time during different evaluation presentations and providing insightful comments, feedback and encouragement during my Ph.D., which has motivated me to probe deeper into my research and has significant contribution in adding new dimensions to my thesis work.

I would also like to acknowledge the Department of Physics, Indian Institute of Technology Delhi, for providing the essential facilities and giving me the opportunity to work here. I also acknowledge the Central Research Facility (CRF) and Nano Research Facility (NRF), IIT Delhi, for providing different experimental facilities used to carry out the work presented in this thesis.

I acknowledge the University Grant Commission (UGC), India, for providing the fellowship and contingency funds to support me during my Ph.D. I am also grateful to Indian Institute of Technology Delhi for providing funds to attend and present my work in international conferences outside India.

I extend my gratitude to all the Advanced Semiconductor Materials and Devices Laboratory members, especially **Dr. Pallavi Aggarwal, Dr. Hardhyan Sheoran, Dr. Tasleem Khan, Dr. Nahid Chaudhary, Ms. Sakshi, Ms. Deeksha, Ms. Sonika, Mr. Shivansh Tiwari** and **Mr. Manish Rautela**, for their support at crucial times and for sharing valuable research inputs. My gratitude extends to **Mr. Rahul Sharma** and **Mr. Hemant Kumar** for their support with different technical and non-technical works during this Ph.D.

My special gratitude extends to my MBE group members. I sincerely thank **Dr. Ashok Kapoor** from the bottom of my heart for all the experimental support, the fruitful discussions regarding my work and for being like a mentor to me throughout this journey. I have been greatly inspired by his curiosity-driven, never-ending learning approach and by the simplicity with which he shares knowledge with everyone, which strongly echoed with my approach. I would also like to thank **Dr. Nand Kumar** for his kind assistance and for sharing his experience in communicating the publications. My special thanks extend to **Dr. Santanu Kandar** for his invaluable support, companionship and most importantly, for sharing such a great level of mutual understanding.

I would also like to acknowledge Solid State Physics Laboratory (SSPL), New Delhi and thank **Dr. Akhilesh Pandey, Dr. R. Raman, Ms. Sharmila** and **Mr. Anand Kumar** for the initial AFM, XRD and FESEM measurements. I would also like to thank **Mr. Biswajit Khan** for his help with the frequency-response photodetection measurements. I express my thanks to **Ms. Lipika**

for helping me with DFT calculations and supporting me at times with different aspects of the Ph.D.

I also express my gratitude to the CRF Sonipat members, especially **Dr. Ganga BG** for sharing her expertise and the valuable discussions with me regarding XPS and beyond, **Dr. Atul Kumar** for the extensive XPS measurements and giving his key support at times for ensuring a smoother functioning of the MBE lab, **Mr. Kshitij Sharma** for giving extra efforts and time with XRD measurements of 2D films. I believe that unsuccessful attempts in research, particularly in the experimental field, are as worthy as successful attempts, contributing to a deeper understanding. Therefore, I extend my thanks to **Dr. Somendra Singh, Dr. Dinesh Kumar, Ms. Neelam and Dr. Veer Singh** for their support with PPMS, TOF-SIMS and glovebox facility.

The acknowledgement would be incomplete without thanking my friends at IIT Delhi, without whom this journey would not have been memorable. The early time spent with Sandeep, Siddharth and Uzair has been short but pleasant. The Pakoda sessions of Santanu, complemented by the performance of Deeksha, will always be cherished as joyful moments. The post-lab sessions, walks and drives in Sonipat campus, especially with *Lipika, Ganga ma'am, Kshitij, Somendra sir, Neelam, Dinesh sir, Atul sir, Sonali ma'am* and *Manjari ma'am*, will be treasured forever.

Finally, no words can truly capture my gratitude to my beautiful family, whose blessings, love and care have been my constant strength. I am grateful to my family for their patience and silent sacrifices, which have carried me through every stage of this Ph.D. This achievement is as much theirs as it is mine.



Kamlesh

New Delhi, India

Date: January 30, 2026

Abstract

The fundamental limitations of bulk silicon at the nanoscale, such as quantum tunneling, short-channel effects, and reduced gate controllability, pose critical challenges to further scaling of semiconductor-based devices. These limitations have motivated the exploration of alternative materials that can extend beyond Moore's law. In this context, two-dimensional (2D) layered materials have emerged as promising candidates owing to their atomic-scale thickness, tunable electronic properties, and potential for seamless heterointegration. Among them, molybdenum ditelluride (MoTe_2) is uniquely suited for integration and device engineering because its semiconducting 2H and semimetallic 1T' phases are separated by only a small ground state energy ($\sim 40\text{--}60$ meV per atom), enabling controllable phase switching as well as access to rich physics beyond the semiconducting aspect. The dual-phase stability, coupled with its narrow bandgap in the near-infrared (NIR) range, makes MoTe_2 a compelling material for next-generation electronics and optoelectronics, as well as for exploring rich material aspects.

In this thesis, molecular beam epitaxy (MBE) has been employed to achieve large-area, phase-pure growth of MoTe_2 thin films on technologically relevant substrates, including silicon and sapphire. Initially, a tellurium-rich pre-wetting growth recipe is combined with careful optimization of growth temperature to achieve the direct integration of crystalline 2H- MoTe_2 on silicon, overcoming the interface challenges posed by dangling bonds. This achievement represents a crucial step toward the integration of 2D semiconductors with established silicon platforms.

Leveraging this foundation, the growth conditions have been established to selectively stabilize semiconducting 2H- MoTe_2 as well as the semimetallic 1T' phase. By systematically tuning the effective concentration ratio of Mo and Te during MBE growth, the study clarifies the existing discrepancies in the literature regarding phase stability. Both the semiconducting 2H and semimetallic 1T' phases, as well as their coexistence, have been achieved

uniformly over centimeter-scale areas in a controllable manner. The findings have shown that the phase engineering in MoTe_2 can be achieved independently of a single growth parameter, such as growth temperature or flux, which is crucial for seamless integration of the hetero phase-based 2D-2D vertical heterostructures and superlattices for tailoring the material properties.

With precise phase control achieved, the thesis advances towards fabricating van der Waals heterostructures, where MoTe_2 is combined with other layered chalcogenides such as MoSe_2 and GaSe . First, scalable layer-by-layer growth of $\text{MoSe}_2/\text{MoTe}_2$ heterostructures is demonstrated, focusing on probing interfacial electronic interaction effects. Using XPS, UPS and Kelvin probe force microscopy, unconventional interfacial charge transfer effects have been observed in the heterostructure band alignment. The tunable probing depth of angle-dependent XPS has been utilized to understand this anomaly, which shows that site-to-site interactions between Se and Te alter the intrinsic chemical bonding near the interface. The Te vacancies pin the MoTe_2 Fermi level, while modified bonding in MoSe_2 raises its valence-band maximum abnormally. Overall, the experimentally observed heterostructure band alignment shows a reduced barrier for the holes, which can be advantageous for bidirectional carrier transport.

Insights from these vacancy-induced carrier doping have further motivated us to carry out intrinsic charge carrier-type control in 2H- MoTe_2 without extrinsic dopants. The chalcogen-to-metal flux has been tuned precisely to achieve n-type behavior in MoTe_2 via Te-vacancies and p-type behavior via Te-rich incorporation. Further, UHV annealing has been demonstrated as an approach to drive p-to-n type transition in MoTe_2 . The Fermi-level shifts in the valence band spectra validate this stoichiometry-driven doping, enabling reliable, wafer-scale ambipolar tuning.

Finally, the potential of the 2D-2D heterostructures has been explored through optoelectronic device demonstrations. The MBE-grown, few-layer $\text{GaSe}/\text{MoTe}_2$ heterostructure has revealed a type-II band alignment with a relatively higher conduction-band offset. The heterostructure-based device

shows a low dark current and asymmetric I-V behavior. The device has achieved a stable and repeatable photoresponse across UV to NIR wavelengths with fast response times on the sub-millisecond scale. Furthermore, the high-frequency optical response of the device is studied, which shows switching of the device up to 3 kHz with an optical response bandwidth of ~2 kHz at 660 nm, highlighting its potential for high-speed optoelectronic applications.

Collectively, this work has established a comprehensive platform for MoTe₂-based device engineering, from scalable synthesis and phase control to interfacial effects in heterostructures, intrinsic ambipolar control and functional heterostructure devices, which significantly contributes to the future integration of 2D materials into practical semiconductor technologies.

सार

नैनोस्तर पर बल्क सिलिकॉन की मूलभूत सीमाएँ, जैसे क्वांटम टनलिंग, शॉर्ट-चैनल प्रभाव तथा गेट नियंत्रण क्षमता में कमी, अर्धचालक आधारित उपकरणों की विस्तार-क्षमता के लिए गंभीर चुनौतियाँ प्रस्तुत करती हैं। इन सीमाओं ने वैकल्पिक पदार्थों की खोज के लिए प्रेरित किया गया है, जो मूर के नियम से आगे बढ़ने की क्षमता रखते हों। इस संदर्भ में द्वि-आयामी (2D) परतदार पदार्थ अपने परमाण्विक-स्तर की मोटाई, नियंत्रित किए जा सकने वाले इलेक्ट्रॉनिक गुणों तथा निर्बाध विषम एकीकरण की क्षमता के कारण अत्यंत आशाजनक प्रत्याशी के रूप में उभरे हैं। इनमें, मोलिब्डेनम डाइटेल्चुराइड (MoTe_2) समाकलन और डिवाइस अभियांत्रिकी के लिए विशिष्ट रूप से उपयुक्त है, क्योंकि इसकी अर्धचालक $2H$ और अर्धधात्विक $1T'$ अवस्थाएँ केवल $\sim 40\text{--}60$ meV प्रति परमाणु की आधार अवस्था ऊर्जा से पृथक होते हैं। यह सूक्ष्म ऊर्जा-अंतर MoTe_2 को नियंत्रित अवस्था-परिवर्तन तथा अर्धचालक गुणों से परे भी समृद्ध भौतिकी तक पहुंच को सक्षम करता है। इसकी द्वि-अवस्था स्थिरता तथा निकट-अवरक्त (NIR) क्षेत्र में संकीर्ण बैंडगैप इसे अगली पीढ़ी के इलेक्ट्रॉनिक्स व ऑप्टोइलेक्ट्रॉनिक्स के साथ-साथ समृद्ध पदार्थीय पहलुओं की खोज के लिए एक अत्यंत आकर्षक पदार्थ बनाते हैं।

इस शोध-प्रबंध में मॉलिक्यूलर बीम एपिटैक्सी (MBE) तकनीक का उपयोग करके तकनीकी दृष्टि से महत्वपूर्ण सबस्ट्रेट्स — जैसे सिलिकॉन (Si) और सैफायर (Al_2O_3) — पर MoTe_2 की विस्तृत क्षेत्रफल और शुद्ध अवस्था वाली पतली परतों की वृद्धि हासिल की गई है। प्रारंभ में, सिलिकॉन पर क्रिस्टलीय $2H\text{-MoTe}_2$ के प्रत्यक्ष एकीकरण को प्राप्त करने के लिए परत निर्माण तापमान के सावधानीपूर्वक अनुकूलन के साथ एक टेल्यूरियम-समृद्ध पूर्व-प्रसंस्करण प्रक्रिया को जोड़ा जाता है, जिससे सतह के असंतृप्त बंधनों द्वारा उत्पन्न इंटरफेस चुनौतियों पर काबू पाया जा सका है। यह उपलब्धि स्थापित सिलिकॉन प्लेटफार्मों के साथ 2D अर्धचालकों के समाकलन की दिशा में एक महत्वपूर्ण कदम का प्रतिनिधित्व करती है।

इस आधार का लाभ उठाते हुए, परत निर्माण-स्थितियों को इस प्रकार स्थापित किया गया कि अर्धचालक $2H\text{-MoTe}_2$ तथा धात्विक $1T'\text{-MoTe}_2$ अवस्था को चयनात्मक रूप से स्थिर किया जा सके। MBE द्वारा निर्माण के दौरान मोलिब्डेनम (Mo) और टेल्यूरियम (Te) के प्रभावी सांद्रण अनुपात को व्यवस्थित ढंग से नियंत्रित करके, साहित्य में उपलब्ध अवस्था-स्थिरता संबंधी असंगतियों को स्पष्ट

किया गया। दोनों अवस्थाएँ (2H और 1T') तथा उनका सह-अस्तित्व, सेंटीमीटर स्तर पर नियंत्रित रूप से प्राप्त किया गया। यह निष्कर्ष दर्शाता है कि MoTe_2 में अवस्था-अभियांत्रिकी को किसी भी निर्माण पैरामीटर, जैसे तापमान या फ्लक्स से स्वतंत्र रूप से प्राप्त किया जा सकता है, जो 2D-2D ऊर्ध्वाधर हेटरोस्ट्रक्चर तथा सुपरलेट्रिस के निर्बाध एकीकरण हेतु महत्वपूर्ण है।

सटीक अवस्था-नियंत्रण प्राप्त होने के पश्चात् शोध कार्य वैन डेर वाल्स हेटरोस्ट्रक्चर (विषमसंरचना) निर्माण की ओर अग्रसर हुआ, जहाँ MoTe_2 को अन्य परतदार चाल्कोजेनाइड्स (जैसे MoSe_2 और GaSe) के साथ संयोजित किया गया। सर्वप्रथम, $\text{MoSe}_2/\text{MoTe}_2$ हेटरोस्ट्रक्चरों का विस्तारक्षम परत-दर-परत निर्माण प्रदर्शित किया गया, जिसका उद्देश्य इंटरफेस (अंतरफलक) पर इलेक्ट्रॉनिक अंतःक्रिया प्रभावों की जांच करना था। XPS तथा केल्विन प्रोब फोर्स माइक्रोस्कोपी का उपयोग करके हेटरोस्ट्रक्चर बैंड-संरक्षण में असामान्य इंटरफेस चार्ज-ट्रांसफर (आवेश अंतरण) प्रभाव देखे गए। कोण-निर्भर XPS की परिवर्तनीय जांच-गहराई का उपयोग इस असामान्यता को समझने हेतु किया गया, जिसने दर्शाया कि Se और Te के पारस्परिक प्रभाव इंटरफेस के पास आंतरिक रासायनिक बंधन को परिवर्तित करते हैं। टेल्युरियम रिक्तियाँ MoTe_2 के फर्मी-स्तर का स्थिरीकरण करती हैं, जबकि MoSe_2 में संशोधित बंधन उसके वैलेंस-बैंड अधिकतम को ऊपर उठाते हैं। समग्र रूप से प्रयोगात्मक रूप से देखा गया कि प्राप्त हेटरोस्ट्रक्चर बैंड-संरक्षण होल के लिए बाधा को घटाता है, जो द्विदिश वाहक-परिवहन हेतु लाभकारी हो सकता है।

इन होल-प्रेरित वाहक-डोपिंग अंतर्दृष्टियों ने आगे 2H- MoTe_2 में बाहरी मिश्रक के बिना अंतर्निहित विद्युतीय प्रकृति-नियंत्रण की दिशा में प्रेरित किया। चाल्कोजेन-धातु फ्लक्स को सटीक रूप से नियंत्रित करके Te-रिक्तियों द्वारा n-प्रकार चरित्र तथा Te-समृद्ध संरचना द्वारा p-प्रकार चरित्र प्राप्त किया गया। इसके अतिरिक्त, UHV एनीलिंग को MoTe_2 में p-से-n प्रकार संक्रमण को प्रेरित करने की रणनीति के रूप में प्रदर्शित किया गया। वैलेंस-बैंड स्पेक्ट्रा में फर्मी-स्तर का स्थानांतरण इस स्टोइकियोमेट्री-प्रेरित डोपिंग की पुष्टि करता है, जिससे विश्वसनीय, वेफर-स्तरीय द्विध्रुवीय नियंत्रण संभव होती है।

अंततः, ऑप्टोइलेक्ट्रॉनिक उपकरण प्रदर्शनों के माध्यम से 2D-2D विषम संरचनाओं की क्षमता का पता लगाया गया है। MBE-विकसित, कुछ-परतों वाले $\text{GaSe}/\text{MoTe}_2$ हेटरोस्ट्रक्चर ने अपेक्षाकृत उच्च कंडक्शन-बैंड ऑफ़सेट के साथ टाइप-II बैंड-संरक्षण प्रदर्शित किया। हेटरोस्ट्रक्चर-आधारित उपकरण ने कम डार्क करंट (अप्रकाश प्रवाह) और असममित I-V (धारा-वोल्टेज) व्यवहार दिखाया। इस उपकरण ने उप-मिलीसेकंड पैमाने पर तीव्र प्रतिक्रिया समय के साथ पराबैंगनी (UV) से समीप-

अवरक्त (NIR) तरंग दैर्घ्य में एक स्थिर और पुनरुत्पादक फोटोरेस्पॉन्स हासिल किया है। इसके अलावा, डिवाइस की उच्च आवृत्ति ऑप्टिकल प्रतिक्रिया का अध्ययन किया गया, जिसने 3 kHz तक स्विचिंग तथा ~2 kHz (किलोहर्ट्ज़) की ऑप्टिकल प्रतिक्रिया-बैंडविड्थ प्रदर्शित की है, जो उच्च-गति वाले ऑप्टोइलेक्ट्रॉनिक अनुप्रयोगों के लिए इसकी क्षमता को रेखांकित करता है।

समग्र रूप से, यह कार्य MoTe_2 -आधारित उपकरण-अभियांत्रिकी हेतु एक व्यापक मंच स्थापित करता है — स्केलेबल (विस्तृत) निर्माण और अवस्था-नियंत्रण से लेकर, हेटरोस्ट्रक्चरों में इंटरफेस प्रभावों, द्विध्रुवीय नियंत्रण तथा कार्यात्मक हेटरोस्ट्रक्चर उपकरणों तक — जो व्यावहारिक अर्धचालक प्रौद्योगिकियों में 2D पदार्थों के एकीकरण को महत्त्वपूर्ण रूप से अग्रसर करता है।

Table of Contents

Certificate	i
Acknowledgements.....	iii
Abstract.....	vii
Table of Contents	xiii
List of Figures	xviii
List of Tables.....	xxviii
List of Abbreviations	xxix
<i>Chapter 1</i> Introduction.....	1
1.1 From Bulk Limitations to 2D Breakthroughs	2
1.2 Two-Dimensional (2D) Layered Materials	2
1.2.1 Classification of 2D Materials.....	3
1.2.2 Transition Metal Dichalcogenides and Two-Dimensional Effects ...	5
1.3 Preparation methods for 2D TMDC materials.....	6
1.3.1 Top-Down Techniques.....	7
1.3.2 Bottom-Up Techniques.....	8
1.3.3 MBE as a Frontier Technique for 2D Material Growth	10
1.4 Van der Waals Epitaxy	12
1.5 Molybdenum Ditelluride (MoTe ₂): A Polymorphic 2D Material.....	13
1.6 Phase Engineering of 2D TMDC Materials.....	15
1.6.1 Doping and Alloying.....	15
1.6.2 Strain Engineering	15
1.6.3 Electrical Field Modulation.....	16
1.6.4 Thermal and Laser-Induced Phase Transitions	16
1.6.5 Phase-Selective Synthesis	17

1.7 Charge Transfer in TMDC Heterostructures and Interfacial Effects ...	17
1.8 Thesis Overview	18
<i>Chapter 2</i> Experimental Techniques for Growth and Characterization	21
2.1 Synthesis Technique: Molecular Beam Epitaxy	22
2.1.1 Components of the MBE system.....	23
2.1.2 Growth Parameters	26
2.1.3 Calibration of the Material Flux (BEPs) and Substrate Temperature	27
2.2 Characterization Techniques	29
2.2.1 Reflection High-Energy Electron Diffraction (RHEED)	29
2.2.2 Raman Spectroscopy.....	33
2.2.3 X-ray Photoelectron Spectroscopy (XPS)	35
2.2.4 Atomic Force Microscopy and Kelvin Probe Force Microscopy	39
2.2.5 X-Ray Diffraction (XRD)	42
2.2.6 Spectroscopic Ellipsometry	45
2.2.7 Transmission Electron Microscopy (TEM)	48
2.2.8 Photodetection measurements.....	50
<i>Chapter 3</i> Van der Waals Epitaxy of Phase-Pure 2H-MoTe ₂ on Silicon: Direct Integration Without a Buffer Layer	54
3.1 Introduction	55
3.2 Experimental.....	56
3.2.1 Pre-growth methods	56
3.2.2 Characterization techniques.....	57
3.2.3 Methodology for buffer-layer-free MoTe ₂ growth.....	58
3.3 Results and Discussion	59
3.3.1 RHEED analysis	60
3.3.2 Raman spectra analysis	61

3.3.3 Spectroscopic ellipsometry	63
3.3.4 XRD analysis	64
3.3.5 AFM analysis	65
3.3.6 XPS analysis	68
3.4 Conclusions	71
<i>Chapter 4 Phase Engineering of MoTe₂ on Sapphire (0001) for Selective Growth of few-layer 2H- and 1T'-MoTe₂</i>	72
4.1 Introduction	73
4.2 Experimental.....	75
4.2.1 Thin film growth	75
4.2.2 Characterization techniques.....	76
4.3 Results and Discussion	77
4.3.1 Structural-phase engineering.....	77
4.3.2 Electrical characterization of semiconducting and semimetallic behavior	84
4.3.3 Chemical bonding state analysis and film-stoichiometry mediated phase evolution	85
4.3.4 Crystalline quality and phase uniformity.....	87
4.3.5 Possible mechanisms governing the Phase change behavior	92
4.3.6 Symmetry-dependent morphological feature.....	94
4.4 Conclusions	97
<i>Chapter 5 Interfacial Bonding Alterations and Charge Transfer-Mediated Effects in MBE-grown MoSe₂/MoTe₂ Heterostructure</i>	98
5.1 Introduction	99
5.2 Experimental.....	100
5.2.1 Thin film growth	100
5.2.2 Material characterization	101

5.2.3 Charge-transfer-study experiments	102
5.2.4 Theoretical calculations	102
5.3 Results and Discussion	103
5.3.1 Large-area growth of vertical heterostructures (trilayer MoSe ₂ /MoTe ₂).....	103
5.3.2 Heterostructure charge transfer study: SKPFM and valence band spectra	106
5.3.3 Origin of different charge transfer processes: XPS core level spectra and energy shifts	111
5.3.4 Interfacial contributions to the unconventional energy shifts: Angle-dependent XPS	114
5.3.5 Modification of band-edge states in MoSe ₂ : DFT calculations....	118
5.4 Conclusions	120
<i>Chapter 6 Growth Process-Driven Modulation of Ambipolar Electrical Characteristics in Few-Layer 2H-MoTe₂</i>	121
6.1.1 Introduction.....	122
6.2 Experimental.....	123
6.2.1 Film growth and annealing.....	123
6.2.2 Characterization techniques.....	123
6.3 Results and Discussion	124
6.3.1 Mo and Te-flux variation effect on the film quality	124
6.3.2 Modulation of the electrical ambipolar nature of MoTe ₂	127
6.3.3 Electrical transport measurements for carrier type verification .	130
6.3.4 Annealing effect on the modulated ambipolar nature.....	131
6.4 Conclusion.....	133
<i>Chapter 7 Large Area Fabrication of GaSe/MoTe₂ Heterostructures for High-Speed Broadband Photodetection</i>	134
7.1 Introduction	135

7.2 Experimental.....	136
7.2.1 Heterostructure growth.....	136
7.2.2 Material characterization	136
7.2.3 Device fabrication and photodetection measurements	137
7.3 Results and Discussion	137
7.3.1 Large-area growth of GaSe/MoTe ₂ heterostructure	137
7.3.2 Heterostructure band alignment	140
7.3.3 Photodetection study.....	142
7.4 Conclusions	147
<i>Chapter 8 Summary and Future Perspectives</i>	<i>149</i>
8.1 Summary	150
8.2 Scope of Future Work.....	153
References	155
Appendix A1	177
Appendix A2	182
Appendix A3	187
Appendix A4	193
Appendix A5	195
List of Publications.....	198
Biodata	203

List of Figures

<i>Figure 1.1 Schematic representing the bulk (3D) crystallographic structures and a single atomic layer (2D) of the crystal.</i>	<i>3</i>
<i>Figure 1.2 The family of 2D materials shows some of the key members of this family, such as graphene, TMDCs, h-BN, black phosphorus (BP), Mxenes and TMMCs with their broader application areas.</i>	<i>4</i>
<i>Figure 1.3 The crystal structure of a bilayer TMDC material, where atoms in each layer are bonded with covalent bonds, while the two different layers are held together with vdW bonding.....</i>	<i>5</i>
<i>Figure 1.4 The schematic of a typical MBE growth chamber with different components.....</i>	<i>11</i>
<i>Figure 1.5 Schematic comparing conventional heteroepitaxy between covalent bonded (3D) materials with the van der Waals epitaxy between the layered (2D) materials, which shows lattice defect creation, such as strain and dislocation, in the case of the former.</i>	<i>13</i>
<i>Figure 1.6 Planar view and side view of the crystal structures of different phases of a TMDC material, namely 2H, 1T and 1T' phase.....</i>	<i>14</i>
<i>Figure 2.1. The picture of the MBE system installed at IIT Delhi for the growth of 2D TMDCs and other 2D materials. The main growth chamber with different assemblies is highlighted with yellow dotted lines.</i>	<i>22</i>
<i>Figure 2.2 The 3D representation of the MBE growth chamber, with its different components.....</i>	<i>23</i>
<i>Figure 2.3 The picture of different components of the 2D MBE system.....</i>	<i>25</i>
<i>Figure 2.4 (a) Calibration of the substrate temperature using different references, which is here measured using the thermocouple placed behind the molyblock; (b) Calibration of the Mo flux with e-beam emission current and (c) Te flux with the temperature of the effusion cell; (d) Te flux is further approximated using the simplified Arrhenius equation.</i>	<i>27</i>

Figure 2.5 Real space and reciprocal space representations for a 2D crystal and a 3D crystal, which shows that the reciprocal space of a 2D crystal consists of reciprocal rods, while that of a 3D crystal consists of reciprocal points.....30

Figure 2.6 The geometrical representations of RHEED. (a) The top view and (b) side view corresponding to the sample surface show that the diffraction occurs at the points where the reciprocal rods of the sample intersect with the Ewald sphere of the incoming electron beam.31

Figure 2.7 Different components of the RHEED system (from the STAIB instruments), which are attached to the MBE system.....32

Figure 2.8 Schematic representation of different energy transitions between the vibrational and virtual energy states resulting in Raman (Stokes and anti-Stokes) and Rayleigh scattering.33

Figure 2.9 The Raman spectroscopy system from Renishaw, which is used for investigating different crystallographic phases in grown films.35

Figure 2.10 Schematic showing a typical XPS measurement system and the underlying photoelectron ejection process from the core level of a material....36

Figure 2.11 The XPS system from Kratos Analytical, which is used for investigating the chemical bonding, film stoichiometry and valence band edge position.38

Figure 2.12 (a) AFM operation in the contact mode, (b) the feedback loop in the contact mode (edit, referenced from Bruker manual).....39

Figure 2.13 (a) AFM operation in the tapping mode, (b) the feedback circuit in the tapping mode (edit, referenced from Bruker manual).....40

Figure 2.14 The AFM system from Bruker, which is used for investigating the surface topography of the grown film. The system also provides the capability of scanning KPFM, which is used to map the surface potential and calculate the work function.....42

Figure 2.15 The HRXRD system from Panalytical, which is used to investigate the out-of-plane crystallinity of the thicker films.44

Figure 2.16 Schematic representation of a spectroscopic ellipsometry setup..46

<i>Figure 2.17 The spectroscopic ellipsometer from Semilab, which is used to estimate the thickness of the uniformly grown films and to determine the optical constants.</i>	<i>47</i>
<i>Figure 2.18 The high-resolution TEM system from JEOL, which is used to confirm atomic scale crystallographic nature of the grown films using imaging and SAED patterns.</i>	<i>49</i>
<i>Figure 2.19 The photodetection measurements system with a Xenon lamp as a light source, which is used for investigating broadband spectral photoresponse from NIR to UV.</i>	<i>52</i>
<i>Figure 2.20 The modulated-laser-based photodetection setup, which is used for investigating the frequency response of the device for two available light sources (660 nm and 785 nm).</i>	<i>53</i>
<i>Figure 3.1 (a)-(e) The evolution of RHEED pattern of silicon substrate with different annealing temperatures under UHV conditions, showing native-oxide desorption after 850 °C; (f) The complete desorption of native-oxide is further confirmed by the XPS core level spectrum of Si 2p, which was acquired from the grown film on the substrate.</i>	<i>57</i>
<i>Figure 3.2 (a) Observation of the intensity change of the diffraction spot in the RHEED pattern for monitoring the tellurium wetting of the substrate's surface and subsequent MoTe₂ growth; (b) The temperature profile showing the growth strategy used for avoiding interfacial MoSi₂ phase formation.</i>	<i>59</i>
<i>Figure 3.3 (a)-(c) RHEED patterns of the MBE grown MoTe₂ over Si(111) for different growth temperatures, in which the spacing between the RHEED streaks corresponds to the lattice spacing of 2H-MoTe₂ along the AC edge; (d) The top view and (e) side view of the stacking orientation between Si(111) and 2H-MoTe₂ with the armchair (AC) edge (<1120> direction) of the latter aligned along the zigzag (ZZ) edge (<112> direction) of the former to minimize the lattice mismatch (The lattice spacings are calculated using the lattice parameters taken from the reference ¹³².</i>	<i>60</i>
<i>Figure 3.4 Raman spectrum of the as-grown MoTe₂ films for different temperatures showing the presence of A_{1g} and E¹_{2g} vibration modes</i>	

corresponding to its 2H phase, which indicates a pure 2H phase over a wide range of growth temperatures. Energy shifts are observed in the Raman modes at different temperatures, which are indicated by the vertical dashed lines. .62

Figure 3.5 (a)-(c) The measured spectra of the spectroscopic parameters Ψ and Δ for the grown films at different growth temperatures, which are fitted with the modelled values. The thickness and roughness of the film are then extracted from the model. (d) The refractive index of MoTe_2 , determined from the fitted model as a function of energy.64

Figure 3.6 (a) XRD pattern of ~ 16.4 nm thick MoTe_2 grown over Si(111) at 450 °C. The occurrence of only the c-family of planes of 2H- MoTe_2 shows an out-of-plane oriented growth. (b) The ω -rocking curve corresponding to the (002) diffraction peak, showing a small FWHM value of 0.20° , indicating highly oriented growth.65

Figure 3.7 (a)-(c) Large-area AFM images for different growth temperatures, showing undergrowth regions at the higher growth temperature; (d)-(f) Small-area AFM images with RMS roughness values, showing relatively higher roughness at the lower growth temperature.66

Figure 3.8 High-resolution AFM images with corresponding line profiles for investigating grain size variation at different growth temperatures.67

Figure 3.9 (a) XPS survey spectra show the presence of different elements where their relative intensity changes for different growth temperatures correspond to the change in their chemical composition; (b) Mo 3d and Te 3d core level spectra with the binding energy of spin-orbit splitted peaks ($3d_{5/2}$ and $3d_{3/2}$) for both Mo and Te corresponding to the 2H phase of MoTe_2 at all growth temperatures; (c) Fitted core level spectra for Mo3d and Te3d demonstrating the presence of different chemical states of the present materials.....69

Figure 4.1 Raman spectra confirming the presence of different phases in the grown MoTe_2 films (a) for different growth temperatures with fixed Te and Mo fluxes (set A) and (b) for different Mo fluxes with a fixed growth temperature

and Te flux (set B). The other growth parameters for the respective figures are given in set A and set B in Table 4.1..... 78

Figure 4.2 (a) Raman spectra confirming the presence of different phases in the grown MoTe₂ films for different Te fluxes (set C), with a fixed growth temperature and Mo flux (set C), (b) Phase evolution for MoTe₂ with Te:Mo flux ratio, which is achieved using Mo (set B) and Te (set C) flux variation independently..... 79

Figure 4.3 (a) Raman spectra for the MoTe₂ films grown at different growth temperatures (set D) with a constant but higher tellurium flux than that was chosen in set A, (b) The contribution of effective concentration ratio is demonstrated by the growth temperature-dependent phase change behavior for lower and higher Te:Mo flux ratio, which shows that a higher flux ratio drives the temperature of pure 2H phase regime to a higher value.82

Figure 4.4 Raman spectra and corresponding AFM images of tellurium-rich MoTe₂ films, confirming Te-nanorods-like structures in the grown film. For different films, the phonon modes corresponding to the Te-rich structures are accompanied by 2H and 1T' phase Raman modes separately, which shows that these vibration modes are independent of the two phases. Also, the relative contribution of these vibration modes (reflected by the peak intensity) in the Raman spectra of 2H- or 1T'-MoTe₂ film follows the density of Te-nanorods in the AFM image, which confirms that these Raman modes correspond to Te-rich structures only..... 83

Figure 4.5 Temperature-dependent resistivity measurements for 2H and 1T' phases of the grown MoTe₂ films, which show a distinct resistivity profile and characteristic features of semiconducting and semimetallic phases, respectively.....85

Figure 4.6 XPS results showing core level spectra of Mo 3d and Te 3d for (a) 1T'-MoTe₂ and (b) 2H-MoTe₂ films grown at two different temperatures. The obtained spectra are deconvoluted to find the contribution of different oxidation states. The stoichiometric is calculated based on the peak area corrected by the corresponding relative sensitivity factor.86

Figure 4.7 (a) XRD patterns taken in the θ - 2θ (gonio) mode for a 10-layer thick 2H-MoTe₂ and (c) 9-layer thick 1T'-MoTe₂ film. The diffraction peaks corresponding to the c-family of planes are obtained in the XRD spectra, indicating an out-of-plane oriented growth. The ω -rocking curve corresponding to (002) diffraction peak of (b) 2H-MoTe₂ and (d) 1T'-MoTe₂ film, with small FWHM values, indicating highly oriented growth..... 88

Figure 4.8 Planer HR-TEM images acquired for (a), (b) 2H and (d), (e) 1T' MoTe₂ films, transferred on the TEM grid after the MBE growth. (c), (f) The corresponding SAED patterns for the two phases confirm distinct diffraction patterns based on the different symmetries of the two phases. 89

Figure 4.9 Raman mapping of (a), (b) a pure 2H-MoTe₂ and (c), (d) a pure 1T'-MoTe₂ films, showing peak area and peak position mapping corresponding to E_{12g} mode of 2H-MoTe₂, and (c), (d) the B_g mode of 1T'-MoTe₂ for investigating small-area phase uniformity. The Raman mapping confirms a uniform phase distribution for both the 2H and 1T' phases of MoTe₂. 90

Figure 4.10 Raman spectra taken from multiple positions across the grown films (as indicated by circles in the camera image of the centimeter-scale grown films) for (e) 2H-MoTe₂ and (f) 1T'-MoTe₂ films. The obtained multipoint Raman spectra confirm the large area phase uniformity of both phases. 91

Figure 4.11 KPFM results show surface potential mapping and the calculated work function values for the grown MoTe₂ films with decreasing flux ratio (Te:Mo). The attached histograms show the distribution of the surface potential value across the surface. A decrease in the work function is observed with increasing tellurium vacancies. 93

Figure 4.12 (a) Large area (15 × 15 μm²) and (b), (c) small area (5 × 5 μm² and 1 × 1 μm²) AFM images of 2H-MoTe₂ confirming the highly uniform nature of the grown film in its 2H phase with a smooth surface. The schematics show the arrangement of atoms on the top surface of (d) 2H and (e) 1T' phase of MoTe₂. 94

Figure 4.13 AFM images of 1T' phase dominant MoTe₂ films showing the triangular surface features in both high and low flux ratio regimes. Large area

AFM images (a), (b), (d) and (e) show the dense network of these triangular regions and defects in the grown films. The triangular features in the 1T' phase are marked using dashed lines in the smaller area AFM images (c) and (f). ..96

Figure 5.1 (a) RHEED patterns showing streaky diffraction pattern corresponding to the grown MoTe₂ and (b) MoSe₂/MoTe₂, (c) The optical image taken on the edge of the uniformly grown vertical heterostructure (the two squared locations represent the two different positions where SKPFM measurements are performed), (d) appearance of the RHEED intensity oscillations confirming layer-by-layer growth of MoTe₂ and (e) MoSe₂ on MoTe₂, (f) Raman spectra of individual MoTe₂ and MoSe₂ and (g) MoSe₂/MoTe₂ heterostructure confirming their 2H phases, (h) AFM height image of MoSe₂/MoTe₂ and (i) reverse stacked MoTe₂/MoSe₂ with height profiles drawn at the step-edge confirming the thicknesses of grown films.105

Figure 5.2 SKPFM images show surface potential mapping with attached histogram profile for individual materials (a) MoSe₂ and (b) MoTe₂; (c) Valence band spectra of individual materials, in which the small humps marked by dashed circles originate from the mirror grain boundaries (MGBs) in MoTe₂, (d) The high-resolution spectra, taken around the valence band edge of MoSe₂ and MoTe₂.....107

Figure 5.3 (a) Band diagrams of individual MoSe₂ and MoTe₂ before heterostructure formation, depicting possible pathway for interlayer charge transfer (ILCT), based on the relative positions of different energy levels, (b) MoSe₂/MoTe₂ heterostructure band alignment, which is predicted based on conventional ILCT between the individual layers (the upwards/downwards arrows show the predicted change in the energy difference between different energy levels due to the ILCT process after the heterostructure formation). .108

Figure 5.4 SKPFM images showing surface potential mapping with attached histogram profile for vertical heterostructures (a) MoSe₂/MoTe₂ and (b) MoTe₂/MoSe₂. (c) The plot shows surface potential and corresponding work function values for individual materials and vertical heterostructures. (d) The 3D SKPFM image taken over a 30 × 30 μm² area at the lateral heterojunction step-edge of MoSe₂/MoTe₂ and (e) MoTe₂/MoSe₂ heterostructures (the insets

show the corresponding 3D AFM height images at the same hetero step-edge);
(f) Valence band spectra showing the comparative shifts of the valence band edge in the heterostructure compared to the individual materials. 110

Figure 5.5 XPS core level spectra of (a) Mo 3d, Te 3d in MoTe₂, (b) Mo 3d, Se 3d in MoSe₂ and (c) these three core levels in the MoSe₂/MoTe₂ heterostructure, all taken at the normal emission angle. The experimentally observed spectra (represented by circles) are fitted using the peak sum (solid black line) of different components corresponding to different bonding states (represented by colored solid lines). 112

Figure 5.6 Schematic representation of angle-dependent XPS depicting different effective photoemission depths at normal emission and 30° emission. 114

Figure 5.7 (a) AD-XPS core level spectra of Te 3d, Mo 3d and Se 3d, taken at 30° emission angle and fitted using different bonding states to quantify individual contributions of these states, (b) Relative changes in the ratio of different components taken at normal (90°) emission and 30° emission, calculated using RSF-corrected areas of different peaks (c) experimentally observed band alignment for MoSe₂/MoTe₂ heterostructure based on the obtained work function and VBM values for the heterostructure. 116

Figure 5.8 Density of states (DOS) spectra of pristine MoTe₂ (red) and MoTe₂ with Te vacancies (black). The presence of Te vacancies induces localized defect states just below the conduction band minimum. 117

Figure 5.9 DFT calculations mapping the partial density of states of (a) Se and (b) Mo in MoSe₂, showing major contributions from Se 4p orbitals and Mo 4d orbitals to the valence band edge states, (c) Total density of states of MoSe₂ with the individual contribution of Se and Mo, (d) DFT-calculated band-structure of MoSe₂. 119

Figure 6.1 2D and 3D AFM images showing the effects of (a), (b) a higher Mo flux and (c), (d) a lower Mo flux on the film quality, confirming that a lower Mo flux leads to a better film quality with lower surface roughness. 125

Figure 6.2 RHEED analysis for (a), (b) a higher and (c), (d) a lower Mo flux. Sharper RHEED streaks are obtained for (c) a lower Mo flux compared to (a) a

higher Mo flux, which confirms a better crystalline quality of the former. (d) RHEED oscillations are obtained for lower Mo flux, indicating a perfect layer-by-layer growth, and (b) vanishes for increased Mo flux. 126

Figure 6.3 (a) AFM image with height profile across the substrate-film step-edge for determining the thickness of the grown MoTe₂ films. (b) Raman spectra of the grown films show the presence of Raman-active vibrational modes corresponding to the 2H phase of MoTe₂ for the three growth sets..... 127

Figure 6.4 (a), (d), (g) Mo 3d and (b), (e), (h) Te 3d core level spectra showing the relative contribution of different chemical bonding states for the grown films. (c), (f), (i) valence-band spectra for the grown MoTe₂ films with different film stoichiometry to determine the position of the valence-band edge with respect to the Fermi level for these films..... 128

Figure 6.5 (a), (b) Resistivity and (c), (d) Hall measurements for the p- and n-MoTe₂ films, to validate the previous Fermi level positioning-based electrical nature of the two films. The positive and negative slopes of the Hall coefficient confirm the p-type and n-type nature of the grown films, respectively. 130

Figure 6.6 XPS valence band spectra for the two sets of annealing, showing the effect of (a), (b) UHV annealing at 600 °C in the absence of Te flux, (c), (d) under the presence of a low Te flux and (e) under the presence of a high Te flux. The relative shifts between the valence band edge and the Fermi level represent the change in the electrical nature of MoTe₂ films. 132

Figure 7.1 (a) Side view of the GaSe and MoTe₂ crystal lattice, (b) Large-area optical image of GaSe/MoTe₂ heterostructure taken at lateral edge to confirm large area uniformity of both grown materials in the heterostructure, (c) Raman spectroscopy taken on the GaSe/MoTe₂ heterostructure, which shows Raman modes corresponding to the ε-phase of GaSe and 2H-phase of MoTe₂. 138

Figure 7.2 (a) AFM and (b) RHEED images of MoTe₂, showing a smooth film surface and sharp RHEED streaks, while (c) AFM and (d) RHEED images for GaSe show relatively higher surface roughness and elongated RHEED spots instead of streaks, indicative of a 3D island surface. 139

Figure 7.3 XPS core level spectra showing the presence of different chemical bonding states; (a) Mo 3d and (b) Te 3d core levels taken for MoTe₂, and (c) Ga 3d and (d) Se 3d core levels taken for GaSe. The acquired spectra are deconvoluted using peak-fitting to extract contributions from the individual components.....140

Figure 7.4 (a) KPFM image, mapping the surface potential for the heterostructure materials, which are used to calculate the work functions of the materials. (b) Valence band spectra taken for MoTe₂ and GaSe, which are used to measure the valence band edge position from the Fermi level, (c) The heterostructure band diagrams of GaSe and MoTe₂ before contact, (d) Heterostructure band alignment of GaSe/MoTe₂ after contact.....141

Figure 7.5 Heterostructure band-bending and qualitative carrier transport behavior across the heterostructure interface under (a) positive bias and (b) negative bias, applied on GaSe, indicating a high barrier for electron transport from the MoTe₂ side to the GaSe side under positive bias142

Figure 7.6 (a) The schematic showing the heterostructure-based device, (b) I-V characteristics of the device under dark and different wavelength illuminations, showing photoresponse from NIR to UV regime, (c) the temporal behavior is investigated at different wavelengths using the I-t curves, showing a stable and repeatable photoresponse of the device at all wavelengths.143

Figure 7.7 Optical power-dependent photoresponse of the device at 380 nm, 600 nm and 1100 nm covering the UV-Vis-NIR spectral range. The obtained photocurrent and photoresponsivity (at -10 V) are plotted against the incident power to extract the value of the power factor for three excitations.....144

Figure 7.8 High-frequency temporal photoresponse of the device for 660 nm laser illumination modulated at (a) 20 Hz, (b) 100 Hz, (c) 1 kHz and (d) 3 kHz, which shows efficient switching of the device up to 3 kHz frequency.....146

Figure 7.9 (a) Single ON-OFF cycle taken at 100 Hz frequency for 660 nm and (b) 785 nm, used for calculating rise and fall times, which show rise and fall times around 500 μs, (c) Optical response bandwidth determination showing a 3 dB bandwidth of 2 kHz for 660 nm and (d) 1 kHz for 785 nm.147

List of Tables

<i>Table 2.1 Flux calibration for tellurium with cell temperature.....</i>	<i>28</i>
<i>Table 2.2 Flux calibration for molybdenum with e-beam emission current.....</i>	<i>28</i>
<i>Table 4.1 The growth parameters used in different sets of growth for investigating the individual contribution and combined effect of the growth parameters on the phase change behavior.</i>	<i>76</i>
<i>Table 5.1 The MBE growth parameters for the heterostructure growth of MoTe₂ and MoSe₂</i>	<i>101</i>
<i>Table 6.1 The three sets of growth parameters for obtaining MoTe₂ films with different chemical compositions, which are achieved by varying the flux ratio.</i>	<i>127</i>

List of Abbreviations

2D	Two-dimensional
5N	99.999 %
6N	99.9999%
AC	Armchair
AD-XPS	Angle-dependent X-ray photoelectron spectroscopy
AFM	Atomic force microscopy
ALD	Atomic layer deposition
ARPES	Angle-resolved photoelectron spectroscopy
BEOL	Back-end-of-line
BEP	Beam equivalent pressure
CBO	Conduction band offset
CPD	Contact potential difference
CVD	Chemical vapor deposition
DFT	Density Functional Theory
DI	Deionised
DOS	Density of states
EAL	Effective attenuation length
ECR	Effective concentration ratio
FET	Field effect transistor
FWHM	Full-width half-maxima
Gr. Temp.	Growth temperature
HOPG	Highly oriented pyrolytic graphite
ILCT	Inter-layer charge transfer
IMFP	Inelastic mean free path
IPA	Isopropyl alcohol
KPFM	Kelvin probe force microscopy
MBE	Molecular beam epitaxy
MGB	Mirror grain boundary
NIR	Near infrared
PBN	Pyrolytic boron nitride

PLD	Pulsed laser deposition
RGA	Residual gas analyzer
rGO	Reduced graphene oxide
RHEED	Reflection high-energy electron diffraction
RMS	Root mean square
RSF	Relative sensitivity factor
SE	Spectroscopic ellipsometry
SOC	Spin-orbit coupling
STM	Scanning tunnelling microscopy
TMDC	Transition metal dichalcogenide
UHV	Ultra-high vacuum
UV	Ultraviolet
VB	Valence band
VBM	Valence band maxima
VBO	Valence band offset
vdW	van der Waals
XPS	X-ray photoelectron spectroscopy
XRD	X-ray diffraction
ZZ	Zigzag